9-19-2024

Remote Sensing Detection of Growing Season Freeze-Induced Defoliation of Montane Quaking Aspen (*Populus tremuloides*) in Southern Utah, USA

Timothy E. Wright
Utah State University

Yoshimitsu Chikamoto
Utah State University

Joseph D. Birch
Utah State University

James A. Lutz
Utah State University

Recommended Citation

Wright, T.E.; Chikamoto, Y.; Birch, J.D.: Lutz, J.A. Remote Sensing Direction of Growing Season Freeze-Induced Defoliation of Montane Quaking Aspen (*Populus tremuloides*) in Southern Utah, USA. *Remote Sens.* **2024**, *16,* 3477. https://doi.org/103390/rs16183477

remote sensing

MDPI

Article

Remote Sensing Detection of Growing Season Freeze-Induced Defoliation of Montane Quaking Aspen (*Populus tremuloides*) in Southern Utah, USA

Timothy E. Wright [1,*], Yoshimitsu Chikamoto [1], Joseph D. Birch [2] and James A. Lutz [2]

[1] Department of Plants, Soils and Climate, Utah State University, Logan, UT 84322, USA; yoshi.chikamoto@usu.edu
[2] Department of Wildland Resources, Utah State University, Logan, UT 84322, USA; joseph.cooper@usu.edu (J.D.B.); james.lutz@usu.edu (J.A.L.)
* Correspondence: a00346272@usu.edu; Tel.: +1-435-200-3334

Abstract: Growing season freeze events pose a threat to quaking aspen (*Populus tremuloides* Michx.), leading to canopy defoliation, reduced vigor, and increased mortality, especially for declining montane populations western North America. Detecting the spatial distribution and progression of this damage is challenging due to limited in situ observations in this region. This study represents the first attempt to comprehensively resolve the spatial extent of freeze-induced aspen canopy damage in southern Utah using multispectral remote sensing data. We developed an approach to detect the spatial and temporal dynamics of freeze-damaged aspen stands, focusing on a freeze event from 8–9 June 2020 in southern Utah. By integrating medium- (~250 to 500 m) and high-resolution (~10 m) satellite data, we employed the Normalized Difference Vegetation Index (NDVI) to compare post-freeze conditions with historical norms and pre-freeze conditions. Our analysis revealed NDVI reductions of 0.10 to 0.40 from pre-freeze values and a second flush recovery. We introduced a pixel-based method to evaluate freeze vulnerability, establishing a strong correlation (R values 0.78 to 0.82) between the onset of the first flush (NDVI > 0.50) and the accumulation of 100 growing degree days (GDD). These methods support the potential for retrospective assessments, proactive forest monitoring, and forecasting future risks.

Keywords: aspen; phenology; defoliation; freeze damage; normalized difference vegetation index (NDVI); growing degree days (GDD); change detection; multispectral remote sensing

Citation: Wright, T.E.; Chikamoto, Y.; Birch, J.D.; Lutz, J.A. Remote Sensing Detection of Growing Season Freeze-Induced Defoliation of Montane Quaking Aspen (*Populus tremuloides*) in Southern Utah, USA. *Remote Sens.* **2024**, *16*, 3477. https://doi.org/10.3390/rs16183477

Received: 26 July 2024
Revised: 13 September 2024
Accepted: 16 September 2024
Published: 19 September 2024

1. Introduction

Quaking aspen (*Populus tremuloides* Michx.) is widely distributed across North America and adapted to various climates, including the diverse environments of mountainous terrain in western North America [1–4]. However, significant declines in montane stands have been observed over the past few decades in the western United States [5–7]. Growing season defoliation following the initial leaf flush leads to stress due to the extra carbon expenditure required for a second flush, resulting in canopy dieback, reduced seasonal growth, and even mortality [5,7–10]. The primary causes of aspen defoliation include biotic agents such as herbivory, insect infestations, and diseases, alongside abiotic stresses like drought and spring freezes [7,11–14]. Understanding the causes of these defoliation events is crucial for developing management and mitigation strategies to ensure the sustainability and recovery of aspen populations and associated ecosystems [15]. In addition, a warming climate poses a heightened risk of freeze-induced defoliation due to an earlier onset of the growing season, assuming the frequency of freeze events remains constant [2,6,7,16]. The impacts of these events are expected to vary across different climate zones and elevational gradients [2,7], which complicate research and management planning.

While freeze damage following the spring leaf flush is recognized as a cause of defoliation, specific details such as the geographic scope of impacted areas and the patterns of these events within the context of a changing climate remain understudied. This gap in knowledge is due to constraints within the observational network, challenges in accessibility, and the sporadic occurrence of freeze events [2,7,8,10]. In Utah, aspen defoliation incidents have been linked to freezing temperatures during the growing season, with recorded events in years such as 1865, 1919, 1954, 2007, and most recently, 2020 [2,8,17]. However, detailed data on the location, timing, and scale of aspen damage from these events are scarce.

Tree-ring analysis has been a valuable tool for characterizing these defoliation events. Abnormally pale or white rings have been correlated with factors such as unusually cool summers [18–20], insect defoliation [21–24], or their combined effects [25], and form as a result of severe defoliation early in the growing season [26]. Severe freeze-induced defoliation of aspen has also resulted in these white rings [2,17]. However, the limited sample size and uneven distribution of tree-ring data prevent comprehensive spatial and temporal assessments of the effects of freeze events on aspen populations, especially concerning canopy vulnerability following spring budburst and the first leaf flush [27].

Given the limitations of tree-ring analysis in capturing the spatial and temporal dynamics of freeze events, remote sensing technologies have emerged as valuable tools for more comprehensive monitoring. The Normalized Difference Vegetation Index (NDVI) has been widely utilized to assess vegetation health and seasonal phenology, including the onset of spring growth or the first flush of leaves [28–30]. This capability has been available since at least the launch of the Advanced Very High-Resolution Radiometer (AVHRR) in the early 1980s, which provided nearly daily phenology data [30], and later, the Moderate Resolution Imaging Spectrometer (MODIS) [4,27,31,32]. These advancements have enabled at least a coarse analysis of the spatial distribution and timing of phenological events. Numerous studies have documented freeze damage using remote sensing to assess vineyards [33,34], temperate forests [35], deciduous tree species in Slovenia and eastern Hungary and Iberian Beech [36–38], and crops such as rapeseed [39] and winter wheat [40]. These studies highlight the potential of remote sensing to monitor freeze damage across various ecosystems and species, a capability that could be adapted for studying aspen populations in Utah.

Despite these advancements, few studies have specifically analyzed freeze damage to aspen in Utah due to its infrequent occurrence and distinct mountain topography. One study focused on a 2007 freeze event in northern Utah [2], where a significant decline in NDVI was observed following the freeze event, with values falling below those of prior freeze-free growing seasons. These findings, corroborated by field observations and temperature measurements, revealed extensive aspen defoliation in late May of that year, followed by a secondary leaf flush in summer [2]. However, the medium-resolution (~250 m) capabilities of MODIS were limited in identifying stand-level impacts, which may be influenced by local microclimates and topographical variations. Additionally, the standard 16-day compositing period of MODIS data used in the study complicates the differentiation between the immediate effects of freeze damage and the gradual effects of drought. Therefore, to overcome these limitations and accurately monitor freeze-induced damage at the stand level, our work proposes a novel methodological framework that leverages higher resolution satellite data and ground-based observations.

This raises questions about the optimal horizontal resolution or homogeneous stand size needed by satellite platforms to effectively monitor such events. While high-resolution platforms like Landsat 5, 7, and 8, and Sentinel 2 have been employed to detect and map other aspen defoliators using change detection [41–44] and to study phenology [41,45], they have not yet been utilized to detect growing season freeze damage in aspen populations, especially in an area where the species is in decline, like southern Utah.

Freeze events typically only cause damage once vegetation is vulnerable, which necessitates an evaluation of this timing. For aspen, this period begins after budburst and

continues through the first flush and into the growing season [10,46,47]. In addition to field surveys, estimates using temperature data, including the accumulated heat above a certain threshold temperature during the spring measured in growing degree days (GDD) or hours (GDH), have been shown to accurately estimate the onset of spring flush [32,48,49]. Furthermore, the first leaf flush has been connected to remotely sensed NDVI, which strongly correlates with ground-based measurements [50,51]. Rapid increases in NDVI have also been linked to simultaneous rises in accumulated heat [29,51]. This approach facilitates a systematic method using climate and remote sensing data to identify the timing and location of vulnerable stands before a freeze event occurs.

The primary goal of our study is to develop a methodological framework that accurately captures the spatial extent of aspen canopy damage attributable to growing season freeze events in southern Utah, where aspens have been in decline. This framework integrates satellite observations with terrestrial weather station data. We aim to answer the following questions: (1) What is the requisite spatial resolution of satellite data for the reliable detection of aspen canopy defoliation? (2) What are the temporal dynamics of aspen canopy response following freeze events? (3) How does satellite-derived phenology correlate with a growing degree day model based on area temperature readings?

2. Materials and Methods

2.1. Study Area and the 2020 Freeze Event

We evaluated temperature data in central and southern Utah above 2500 m, areas where aspen is the predominant deciduous tree species [1,52,53] (Figure 1). Also, in this region, freeze-damaged aspen leaves were collected from the Utah Forest Dynamics Plot (UFDP) at 3100 m in the Cedar Mountain area of Utah (Figures 1a and 2) in early July 2020 [17], confirming damage in the area. Unusually warm temperatures occurred in May and early June 2020 (Figure 1c), suggesting an early transition from winter dormancy to budburst and initial leaf flush for aspen [4,54]. However, a significant temperature drop of 15 °C noted in Global Historical Climatology Network (GHCN) weather station data [55] occurred on 8–9 June or day of year (DOY) 160–161. Furthermore, widespread subfreezing temperatures around 3000 m were noted in a reanalysis of ERA5 temperature data [56] (Figure 3), and at some surface-based stations, temperatures fell below −3 °C (Table 1). Temperatures in this range are known to cause freeze damage in aspen [10]. This event provides an excellent opportunity to employ data from several satellite platforms to identify freeze-induced aspen defoliation.

Table 1. Global Historical Climatology Network (GHCN) station daily minimum temperatures (°C) recorded from 6–11 June 2020 at sites closest to the time series locations.

Site	Latitude (°N)	Longitude (°W)	Elevation (m)	Daily Minimum Temperature (°C)					
				6-Jun	7-Jun	8-Jun	9-Jun	10-Jun	11-Jun
Black Flat-U.M. CK	38.68	111.60	2884	2.2	−2.2	−3.3	−3.3	−0.6	1.1
Brian Head	37.68	112.86	3040	2.8	−3.3	−5.0	−3.3	3.3	8.3
Clayton Springs	37.97	111.83	3063	1.7	−1.7	−3.3	−3.3	−1.7	1.7
Fish Lake Utah	38.50	111.77	2681	3.3	−1.1	−2.8	−4.4	5.6	3.9
Kolob	37.53	113.05	2806	3.9	−2.2	−3.3	0.0	6.1	6.1
Widtsoe #3	37.84	111.88	2938	3.3	−1.7	−3.3	−2.2	3.3	7.2

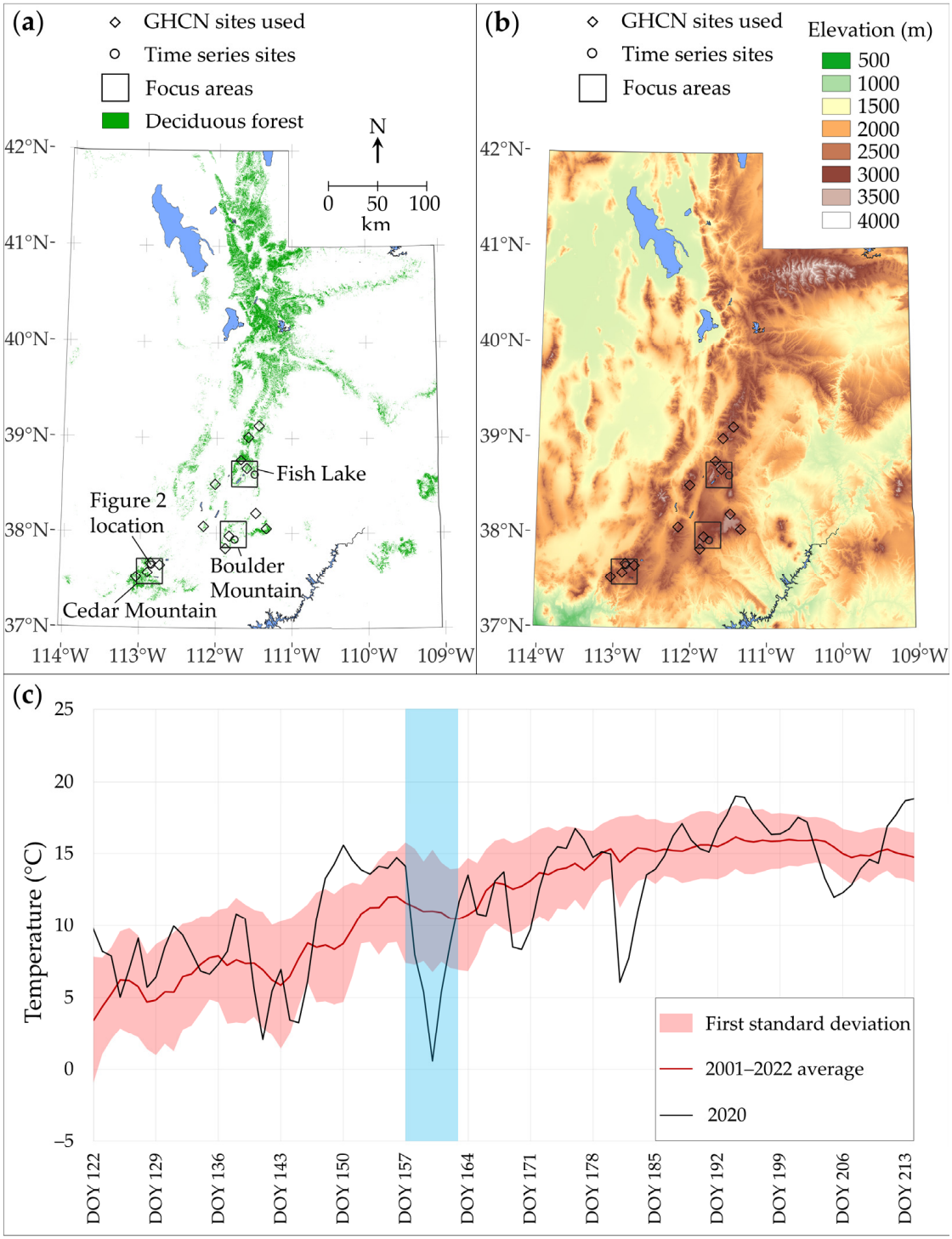

Figure 1. (**a**) Spatial maps of National Land Cover Database (NLCD) deciduous forest land cover in Utah and (**b**) Shuttle Radar Topography Mission (SRTM) at a 30 m resolution elevation. The boxes in (**a**,**b**) represent the focus regions and diamond-shaped markers represent the weather stations used in this study. (**c**) Day of year (DOY) time series of daily mean air temperature, showing the climatological mean (red line), the range of one standard deviation (red shading), and the values in 2020 (black line). The location of the photograph in Figure 2 is indicated. The vertical blue shading highlights the period surrounding the 2020 freeze event represented in Figure 3.

Figure 2. Photo taken in July 2023 by the lead author. The view is towards the Cedar Mountain time series site located in the Utah Forest Dynamics Plot (UFDP). The geographic coordinates of the photograph are 37.6618, −112.8538 and at 3091 m elevation. This location is where aspen leaves with evidence of freeze damage were collected in July 2020.

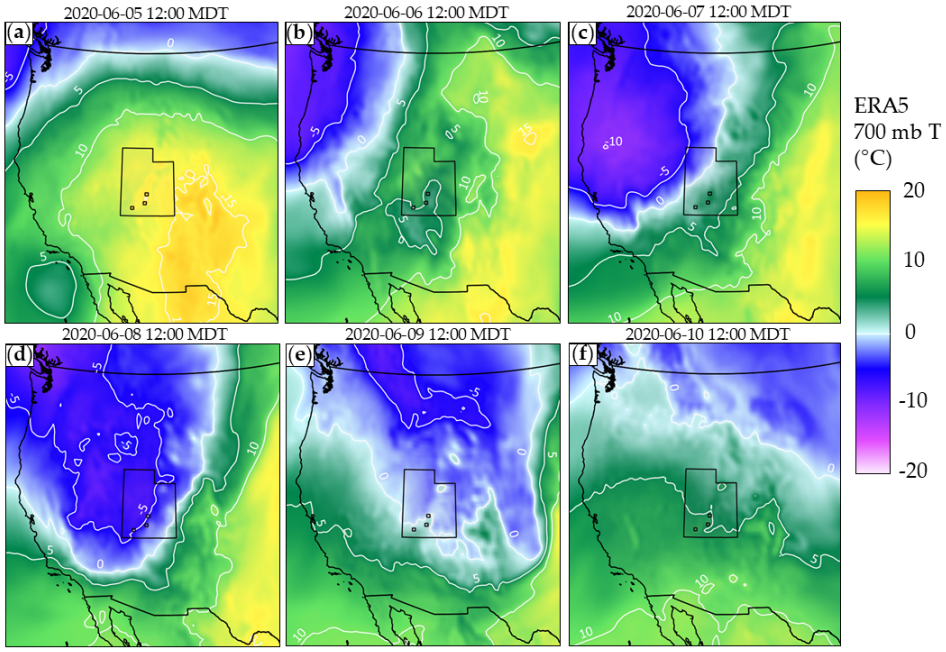

Figure 3. ERA5 reanalysis of temperature at 700 mb centered over Utah (black outline) in the western United States at daily intervals surrounding the freeze event (blue shading in Figure 1c) starting with (**a**) 5 June 2020 at 12:00 MDT (18:00 UTC) and ending 10 June 2020, with 5 °C contours indicated in white. The focus areas of this study are indicated by the small boxes, which are the same areas indicated in Figure 1.

2.2. Satellite Platform Data

We collected multispectral data from three satellite platforms to calculate vegetation health indices (Table 2). These platforms include the Moderate Resolution Imaging Spectrometer (MODIS), built by Raytheon/Santa Barbara Remote Sensing, Goleta, California, USA, aboard the Terra satellite [57,58], the Visible Infrared Imaging Radiometer Suite

(VIIRS), built by Raytheon, El Segundo, California, USA, on the Suomi National Polar-orbiting Partnership (NPP) satellite [59,60], and the Multi-Spectral Instrument (MSI), built by Airbus Defence and Space, Friedrichshafen, Germany, on Sentinel 2a and 2b [61]. We collected MODIS (MOD09GQ.061) daily observation data with a spatial resolution of 250 m, available from February 2000 [62]. Daily VIIRS data (VNP43A), which are 375 m and with data availability beginning in March 2012, were chosen for their continuity with MODIS data [63]. MSI delivers the highest spatial resolution of 10 m, although with a lower revisit frequency of five days (10 days before 2017) and a more limited temporal record (beginning October 2015) for the MSI data obtained [61]. We excluded the Operational Land Imager (OLI) on Landsat 8 due to a much longer revisit frequency of 16 days [64] and a lack of cloud-free observations during the study period.

Table 2. Freely available multispectral satellite imagery from polar-orbiting satellites considered with the periods of record, revisit frequency, spectral bands used for the NDVI calculation, and grid cell resolution.

Satellite (Sensor)	Observation Start	Revisit Frequency	NDVI/EVI Spectral Bands (Wavelength in nm)	Resolution (m)
Suomi (VIIRS)	Mar 2012	Daily	Blue (478–488), Red (600–680), NIR (850–880)	375 (Red, NIR), 750 (Blue)
Terra (MODIS)	Feb 2000	Daily	Blue (459–479), Red (620–670), NIR (841–876)	250 (Red, NIR), 500 (Blue)
Sentinel 2a/2b (MSI)	Oct 2015	10 Days (5 since 2017)	Blue (425–555), Red (650–680), NIR (780–885)	10 (Blue, Red, NIR)

We obtained freely available satellite data online from two main sources. MODIS and VIIRS data were obtained at https://appeears.earthdatacloud.nasa.gov/ (accessed on 8 January 2023) by selecting the geographical area of interest for this study within southern Utah (37°N to 40°N latitude and 111°W to 114°W longitude) and the time span from the observation start through 2022. The results were provided by the server via email notification then downloaded via the provided link to their web-based data acquisition interface. MSI data were obtained at https://console.cloud.google.com/storage/browser/gcp-public-data-sentinel-2/L2 (accessed on 8 January 2023) and by selecting the specific Sentinel 2 tiles covering the study area's focus regions (12SUG, 12SUH, 12SVG, and 12SVH) [65] and spectral band data required. Georeferencing and map calculations required for Sections 2.3–2.6 below were conducted using QGIS 3.24 (https://qgis.org accessed on 8 January 2023).

2.3. Assessing Changes in Vegetation Health

To measure changes in aspen canopy health, we utilized three vegetation health indices for this study: NDVI, EVI, and LAI. We calculated NDVI for all three satellite platforms, while we derived EVI and LAI only from MSI data because of the availability of the requisite spectral bands at matching spatial resolutions. NDVI is a widely employed metric for assessing vegetation health because of its ease of calculation and established use in studies on aspen phenology and freeze response [34,66]. We computed NDVI using the following equation:

$$\mathrm{NDVI} = \frac{\mathrm{N} - \mathrm{R}}{\mathrm{N} + \mathrm{R}} \quad (1)$$

where N represents the near-infrared band, and R represents the visible red band of the electromagnetic spectrum. Although the MODIS NDVI is a proven indicator of vegetation health, cloud cover poses an analytic challenge. To mitigate this, we derived median values from the MOD09Q1 level 3 product, which selects the best pixel from an 8-day composite free of clouds, shadows, and snow based on the lowest viewing angle and highest solar zenith angle [62]. Additionally, we filtered daily data from the MOD09GQ level 2 product to remove pixels with spectral band values indicative of clouds or snow. We found that

these corresponded to NDVI values below 0.4 or the senescent state after the completion of the snowmelt. This is consistent with prior studies of aspen [51,67]. We found that shadows caused erroneously high NDVI values. These were filtered by removing NDVI pixels where band N < 1800 (data range stated as −100 to 16,000) [58]. Although this filtered most shadows, edge effects and blending across pixels prevented the removal of all shadows.

The Enhanced Vegetation Index (EVI), a complementary indicator of vegetation health and phenology, was calculated from MSI data to validate aspen defoliation. It incorporates the red (R), near-infrared (N), and blue (B) spectral bands, which helps reduce atmospheric effects [31,34,66] and is defined by the following equation:

$$\mathrm{EVI} = \frac{2.5(\mathrm{N} - \mathrm{R})}{\mathrm{N} + 6.0\mathrm{R} - 7.5\mathrm{B} + 1.0} \quad (2)$$

We calculated the Leaf Area Index (LAI) as an alternative method of quantifying aspen defoliation, estimating it here from MSI data. It quantifies the ratio of the total photosynthetic canopy leaf area to the ground surface area [68,69]. We utilized a machine learning algorithm in the Sentinel Toolbox available through the EO Browser website linked from https://custom-scripts.sentinel-hub.com/custom-scripts/sentinel-2/lai/ (accessed on 8 January 2023). The algorithm employs an artificial neural network (ANN) to estimate the LAI [69].

Other indices derived from MODIS were considered. The EVI and LAI are available from MODIS, but at a coarser resolution (500 m) that limits target areas and our investigation of the requisite resolution to detect freeze damage. The Enhanced Vegetation Index 2 (EVI2) [70] was considered since, like NDVI, it is available at a 250 m resolution. However, since it is also based on red and NIR bands, it correlates strongly with NDVI [71] and thus would not significantly contribute to this work.

To verify results with the known aspen cover extent, we retrieved data from the National Land Cover Database and extracted the deciduous forest layer (Figure 1a) [72]. These data were processed from multi-year composites of Landsat 8 OLI spectral data [73]. Despite utilizing multiple images, the 16-day Landsat revisit cycle, along with cloud cover and varying viewing angles, posed challenges for accurate land cover classification, achieving a reported accuracy of 78–86% for deciduous forest categorization [74].

2.4. Spatial Analysis 1: Median Deviation Method

To assess the spatial extent and intensity of canopy health changes, we calculated NDVI anomalies from median values for all three satellite platforms for the period of record through the year 2022. We selected 1 July 2020 for the post-event analysis as a clear, cloud-free day occurring approximately three weeks after the freeze event, which is before the reflush of leaves would occur [9,46]. Median NDVI values were computed over a 16-day interval during the growing season (May–July) to ensure a robust sample size. For instance, the median NDVI for 1 July corresponds to 160 samples (16 days × 10 years) for VIIRS, 352 samples (16 days × 22 years) for MODIS, and 18 samples (3 days × 6 years) for MSI. NDVI anomalies on 1 July 2020 were then determined by subtracting these median values and compared across the three satellite platforms for spatial and temporal analyses. This approach aims to effectively highlight the areas of reduced NDVI on the target date (1 July) compared to the average conditions and differentiate defoliation due to the freeze event. A sufficient observation period was required to establish median values and to limit the potential for confounding factors, such as the impact of wildfires. This method also minimizes the noise in NDVI values caused by cloud cover and shading.

2.5. Spatial Analysis 2: Change Detection Method

We employed a change detection approach by comparing NDVI values before and after the freeze dates. We selected 1 July 2020 again as the post-freeze date, as in the previous analysis. The pre-freeze dates were chosen as 6 June 2020 for VIIRS and 1 June 2020 for both MODIS and MSI, which represent the closest clear-sky observations before the freeze

event at Boulder Mountain, Fish Lake, and Cedar Mountain. We also assessed changes in the EVI and LAI for the pre- and post-freeze events in 2020 using MSI data. Detecting the difference or change in the NDVI between the pre- and post-freeze dates is suitable for periods with limited satellite data as it requires only two observation dates; however, the results can be slightly noisy, especially with lower-resolution satellite platforms like VIIRS, as described below.

2.6. A Pixel-Based Method for Temporal Dynamics

To analyze the temporal dynamics of NDVI changes, we employed a pixel-based method of geographically overlapping VIIRS, MODIS, and MSI data. We conducted visual inspections at selected sites near Boulder Mountain and Fish Lake with larger homogeneous aspen stands and Cedar Mountain, a location with a smaller aspen stand surrounded by mixed forest. The areas surrounding these locations were verified using MSI visible color imagery and NDVI data collected before and after the freeze event and then compared with the National Land Cover Database (NLCD) deciduous forest coverage (Figure 1a).

Time series locations and positions of overlapping pixels were selected to minimize the effects of georeferencing or pixel registration errors. For MSI, locations with at least three pixels (10 m resolution) within a homogeneous aspen forest were chosen. This minimized data errors or biases from pixel registration error, which is 3 m for the 10 m resolution bands [75]. Since the average registration error for MODIS is less than 50 m [76], MSI pixel locations were selected so that the MSI pixel was no closer than 70 m from the edge of the MODIS and VIIRS pixels. Although VIIRS geolocation errors are larger than those of MODIS, the average error is less than 75 m, with most falling within 60 m [77]. We deemed this MSI pixel positioning sufficient to reduce potential error due to pixel registration variation between MSI, MODIS, and VIIRS. However, to handle potentially larger errors or offsets in MODIS and VIIRS, especially in high terrain [76,77], the two locations with large homogeneous Boulder Mountain and Fish Lake aspen stands were chosen to be centered over a stand at least 750 m or two VIIRS or three MODIS pixels across. However, the Cedar Mountain location depicted in Figure 2 contains a much smaller stand of only about 100 m across.

The time series NDVIs for the three selected locations were constructed using the selected overlapping VIIRS, MODIS, and NDVI pixels to capture the annual phenology during the spring and summer and compare to climate data. To statistically quantify an average first flush date for comparison with the 2020 values and local climate data, we constructed a 22-year MODIS NDVI (2001–2022) daily time series with the first standard deviation surrounding the spring first flush. It was found that the sharp increase in the NDVI during the spring indicates a green-up or first flush of canopy leaves [50,51,78], which is the target of this comparison.

2.7. Daily Temperature Observations

We obtained daily minimum and maximum temperatures from Global Historical Climatology Network (GHCN) stations in the elevation range of aspen in southern Utah (generally above 2500 m elevation) in and around the three subregions (Figure 1a,b) to cover the 22-year period of 2001–2022 (Table 3). Elevation data were confirmed with station metadata and elevation data from the Shuttle Radar Topography Mission (SRTM) at a 30 m resolution (Figure 1b). We selected the closest stations to the subregions with at least 90% valid data coverage for the same 22-year period as the MODIS NDVI dataset. As a result, we collected data around each subregion, including four stations for Cedar Mountain, five stations for Boulder Mountain, and five stations for Fish Lake. To account for different elevations among stations, we calculated the annual mean climatology of both the minimum and maximum temperature at each weather station by taking the average for the 22-year period when all station data overlapped each other. Next, we adjusted the annual mean climatology for each station to be the same value as the station average for each subregion. From these elevation-adjusted daily minimum and maximum temperatures, we

obtained the daily average for each subregion. The resultant daily mean temperature in each subregion showed 100% data coverage for the 22-year period, which was applied to the growing degree days model (Section 2.6 below). Daily climatological mean temperature by day of year with standard deviations were then calculated from these data (Figure 1 and Table 3).

Table 3. GHCN stations used to determine temperature and GDD data.

Focus Region	Station ID	Station Name	Latitude (°N)	Longitude (°W)	Elevation (m)	Coverage (%)
Boulder Mountain	USS0012L20S	Jones Corral	38.07	112.17	2972	99.13
	USS0011M06S	Clayton Springs	37.97	111.83	3063	98.96
	USS0011M03S	Widtsoe #3	37.84	111.88	2938	98.17
	USS0011M01S	Sunflower Flat	38.05	111.34	3035	97.99
	USS0011L05S	Donkey Reservoir	38.21	111.48	2987	97.58
Fish Lake	USS0012L04S	Box Creek	38.51	112.02	2996	98.67
	USS0011L04S	Black Flat-U.M. CK	38.68	111.60	2884	97.11
	USS0011L01S	Farnsworth Lake	38.77	111.68	2951	99.14
	USS0011K39S	Pickle Keg	39.01	111.58	2926	98.77
	USS0011K31S	Buck Flat	39.13	111.44	2874	98.27
Cedar Mountain	USS0012M14S	Brian Head	37.68	112.86	3040	98.27
	USS0012M13S	Castle Valley	37.66	112.74	2920	97.96
	USS0012M03S	Webster Flat	37.58	112.90	2805	98.87
	USS0013M05S	Kolob	37.53	113.05	2806	99.21

2.8. Growing Degree Days Model

We employed a growing degree days (GDD) model to estimate the progress of aspen growth and development based on daily temperature. Utilizing the daily maximum (Tmax) and minimum (Tmin) temperatures, as described above, we initially calculated growing degrees (GD) by subtracting a selected baseline temperature (Tb) from the daily temperature average, as shown in Equation (3).

$$GD = 0.5(T_{max} + T_{min}) - T_b \quad (3)$$

Typically, a 5 °C baseline temperature is common for aspen phenology assessments in North America, including Utah [1,7,48,79], while a 0 °C baseline may be more suitable for higher-latitude regions like Canada [49]. Subsequently, we accumulated the positive values of growing degrees each day, starting from 1 January (day of year, DOY 1) to a given day (n), defining GDD in Equation (4) as follows:

$$GDD(n) = \sum_{i=0}^{n} MAX[GD_i, 0] \quad (4)$$

Here, GD_i represents the growing degrees for each day, and the MAX[] function selects the maximum value within the brackets, thus setting all negative GD_i values as 0. By applying the adjusted observations with complete data coverage described above, we can estimate GDD for the selected regions appropriately.

3. Results

3.1. Spatial Analysis of Aspen Damage Due to the 2020 Freeze Event

The median deviation method effectively captured declines in the NDVI, demonstrating their abnormal conditions in spatial distribution and intensity of aspen defoliation due to the 2020 freeze event. In the southern Utah region, areas within the elevation range of 2500 m to 3200 m, larger median NDVI values (Figure 4a–c) coincided with the presence of aspen forests and largely overlapped the NLCD deciduous forest areal coverage in this region (see Figure 1a). Comparatively lower post-freeze (1 July 2020) NDVI values across southern Utah were more pronounced regionally in VIIRS and MODIS data (Figure 4d,e)

but were less distinct at this scale in MSI data (Figure 4f). The median NDVI deviation values calculated for aspen stands (Figure 4g–i) showed a notable decrease, ranging from 0.1 to 0.4, when subtracting the 1 July 2020 NDVI from the median for that date, with values 48–80% of the historical median across all satellite platforms.

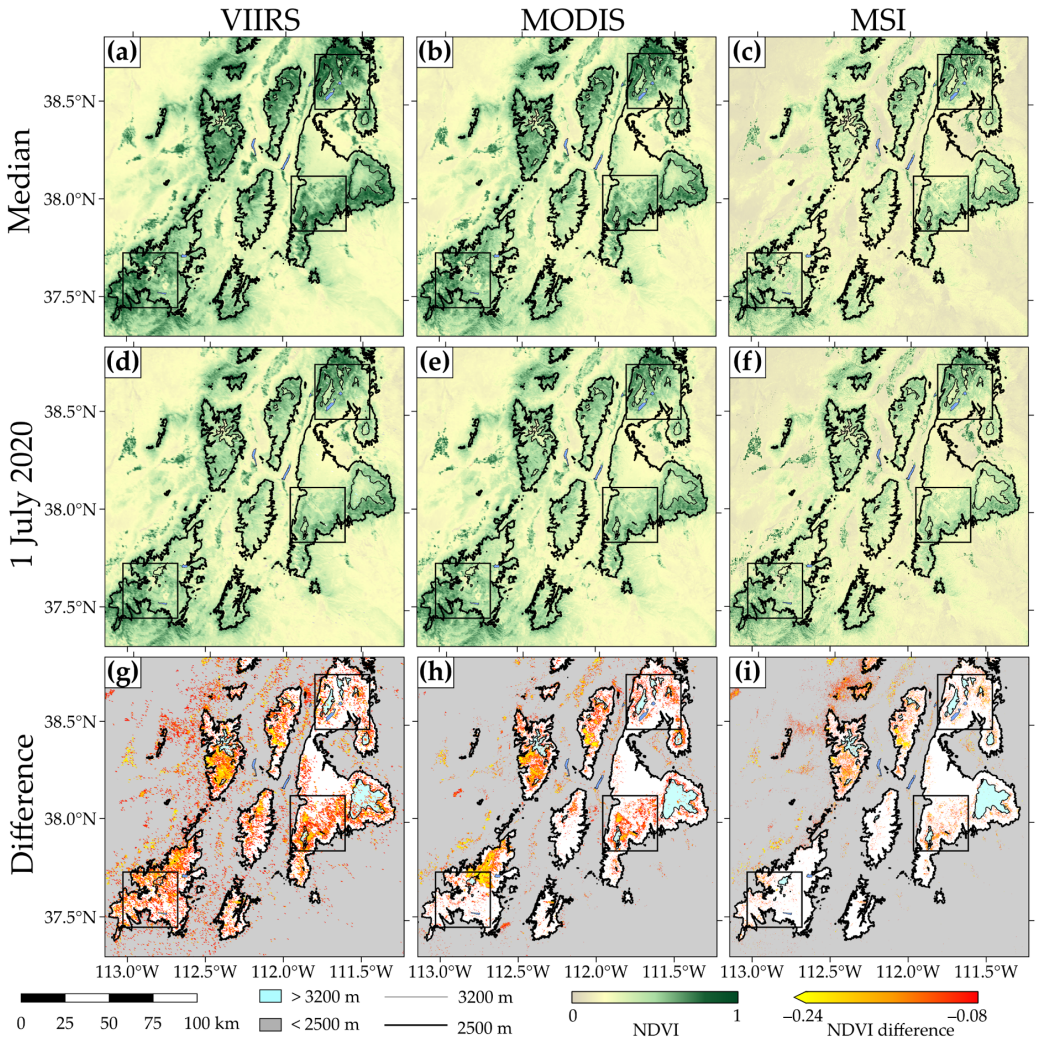

Figure 4. NDVI maps covering the focus area outlined in Figure 1a,b for the median NDVI from 22 June to 8 July for (**a**) VIIRS for 2013–2022, (**b**) MODIS for 2000–2022, and (**c**) MSI for 2016–2022; NDVI on 1 July 2020 for (**d**) VIIRS, (**e**) MODIS, and (**f**) MSI; and the anomaly or difference calculated by subtracting the NDVI of 1 July 2020 from the stated median for (**g**) VIIRS, (**h**) MODIS, and (**i**) MSI. Thin black line contours in (**a**–**f**) delineate elevations at 2500 m and 3200 m. In (**g**–**i**), areas below 2500 m and above 3200 m are shaded gray and light blue, respectively. Boxes indicate the three assessed subregions in Figures 5 and 6.

When the 1 July 2020 deviations from the median were overlaid with the median values for that date and compared across the three focus regions, the results from the different satellite platforms became clearer. As shown in Figure 5, MSI excelled in providing detailed, local, or stand-scale NDVI declines. At Boulder Mountain (Figure 5a–c) and Fish Lake (Figure 5d–f), the large homogeneous areas of aspen between 2500 m and 3200 m exhibited extensive reductions on 1 July 2020 compared to the median. Some of the more expansive areas of reductions are outlined by blue dashed lines. The geographical patterns were similar among all three satellite platforms. However, the larger pixel sizes of VIIRS and MODIS resulted in a broader areal coverage of declines from the median, though the intensity of these declines was not as pronounced as with the MSI values. In contrast,

Cedar Mountain, which has much smaller and less frequent homogeneous aspen stands (Figure 5g–i), showed lower overall coverage and a mismatch among the satellite platforms. For instance, a fire from 2017 was noted in the MODIS data in the northeast corner of the region and is outlined with a black dotted line (Figure 5h). It does not appear in Figure 5g and h due to the position of 2017 early in the VIIRS and MSI periods of record. Another fire later in the period in 2019, was noted in all three platforms (black dotted outline in Figure 5g–i just south of the time series location). Much of the VIIRS data for this area did not align with the data from the other platforms, likely due to the larger pixel sizes and significant distance from the zenith.

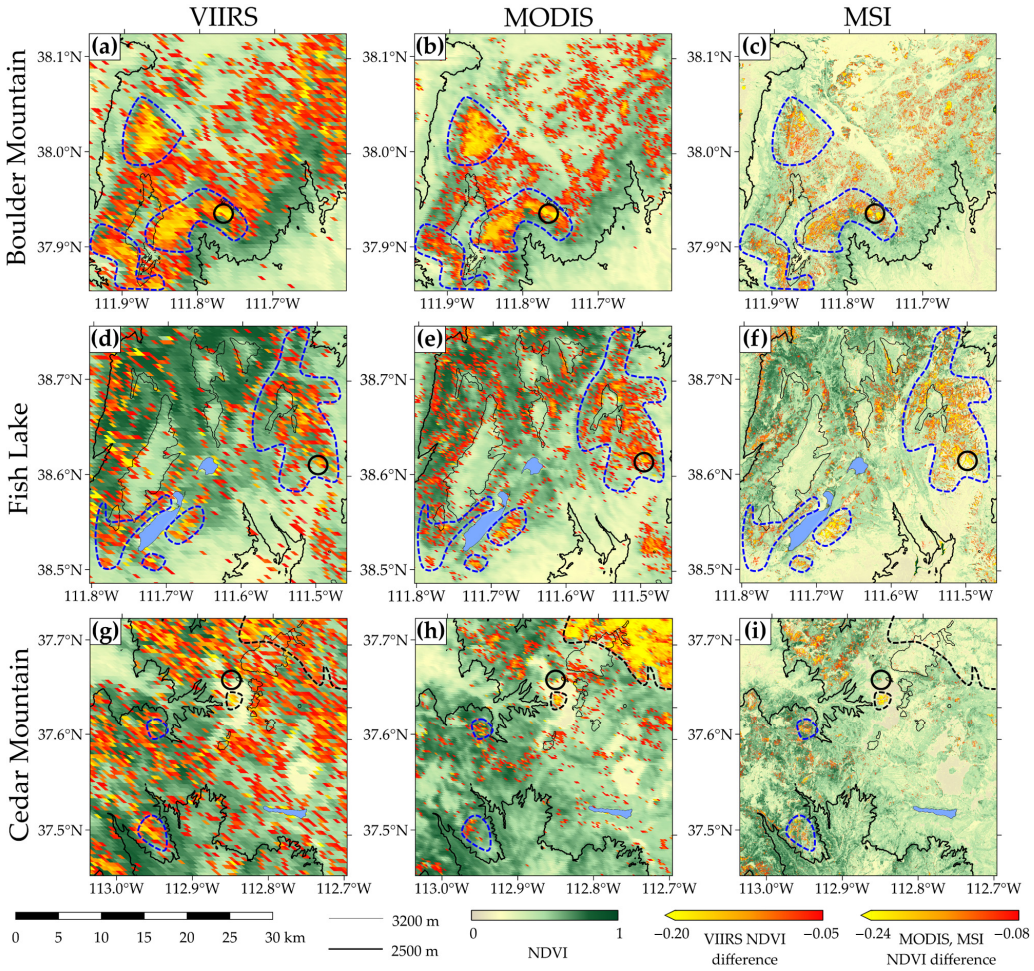

Figure 5. NDVI for 1 July 2020 (green color scale), NDVI difference (yellow-red color scale) from 1 July 2020, and the median NDVI from 22 June to 8 July for the observation periods of 2001–2022 for MODIS, 2012–2022 for VIIRS, and 2016–2022 for MSI at (**a**–**c**) Boulder Mountain, (**d**–**f**) Fish Lake, and (**g**–**i**) Cedar Mountain based on VIIRS (left panels), MODIS (center panels), and MSI (right panels). Contours delineate elevations at 2500 m (thick black lines) and 3200 m (thin black lines). Black circles indicate locations used for NDVI and GDD time series and regression analyses in Figures 9 and 10. The circled location at Fish Lake is the same area as indicated in Figure 8. The NDVI difference color scaling was changed from Figure 4. Areas outlined in blue indicate areas of freeze damage to aspen and areas outlined in black are fire burn scars.

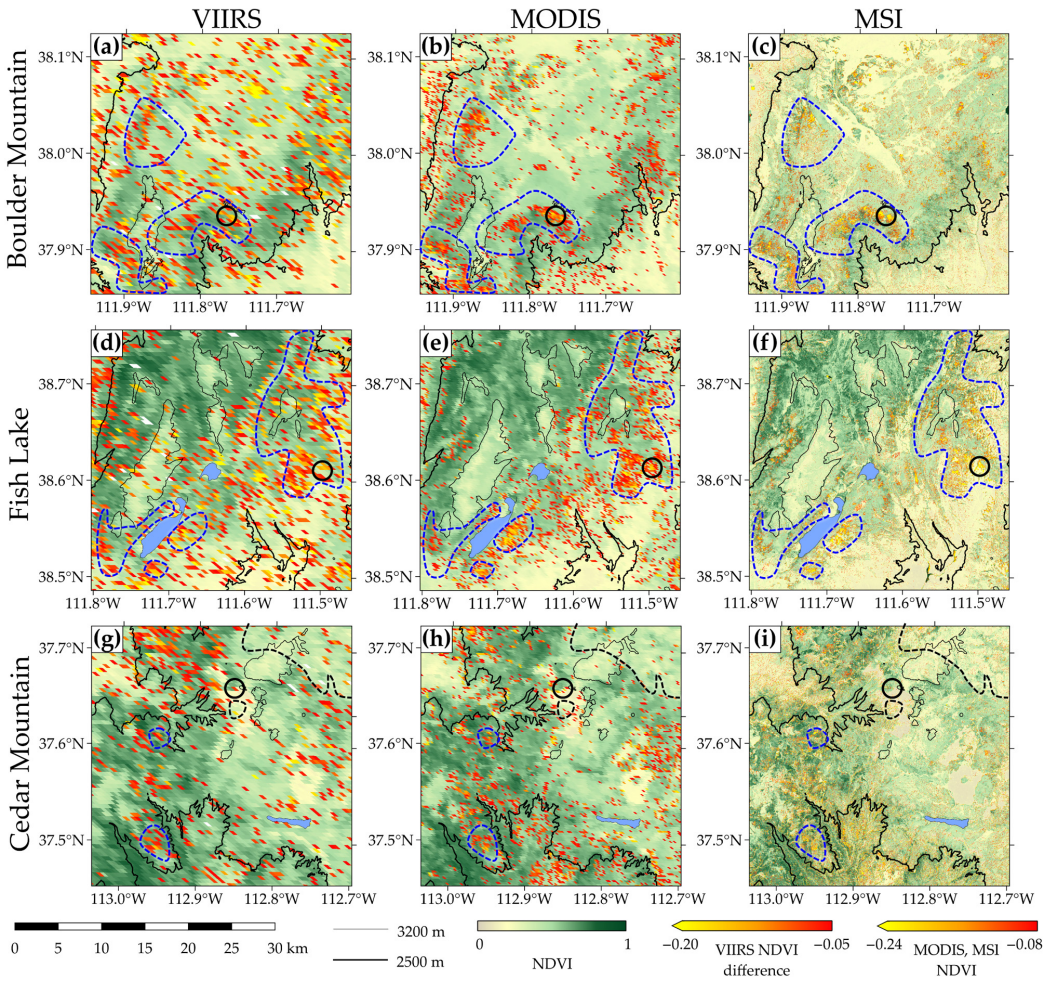

Figure 6. NDVIs for all three satellite platforms on 1 July 2020 overlaid with the NDVI differences of 1 July minus 6 June 2020 for VIIRS (left panels), 1 July 2020 minus 1 June 2020 for MODIS (center panels) and MSI (right panels) at (**a**–**c**) Boulder Mountain, (**d**–**f**) Fish Lake, and (**g**–**i**) Cedar Mountain. Contours delineate elevations at 2500 m (thick black lines) and 3200 m (thin black lines). Black circles indicate locations used for NDVI and GDD regression and time series analyses. Areas outlined in blue indicate areas of freeze damage to aspen and areas outlined in black are fire burn scars.

When change detection using the NDVI was calculated (Figure 6), there was less areal coverage of NDVI declines between 1 June and 1 July 2020 compared to using the median deviation method, but similarities remained across the platforms. At Boulder Mountain (Figure 6a–c) and Fish Lake (Figure 6d–f), declines in the NDVI were also observed in aspen areas within the elevation band between 2500 and 3200 m. Clearer similarities in the change detection method were noted between MODIS and MSI than with VIIRS, particularly in the areas outlined in the blue dashed lines. At Cedar Mountain (Figure 6g–i), the effect of heterogeneous land cover, including smaller aspen areas, was evident, with the larger VIIRS and MODIS pixels inflating the areal coverage of NDVI declines compared to MSI. These results highlight that MODIS (~250 m), and to a lesser extent, VIIRS (~375 m), could resolve the freeze-induced aspen defoliation in the larger homogenous stands, such as Boulder Mountain and Fish Lake. Conversely, in smaller aspen stands or mixed forest areas, like at Cedar Mountain, higher resolution MSI (~10 m) data are required.

A comparison of change detection using the NDVI, LAI and EVI in MSI showed strong similarities in the position and magnitude of the change detected (Figure 7). The spatial distributions and magnitudes of NDVI declines were nearly identical to those of the LAI and EVI, especially in the elevation range between 2500 and 3200 m. It was difficult to find

any significant differences between the indices, which indicated that the simpler NDVI calculation was sufficient for this type of investigation.

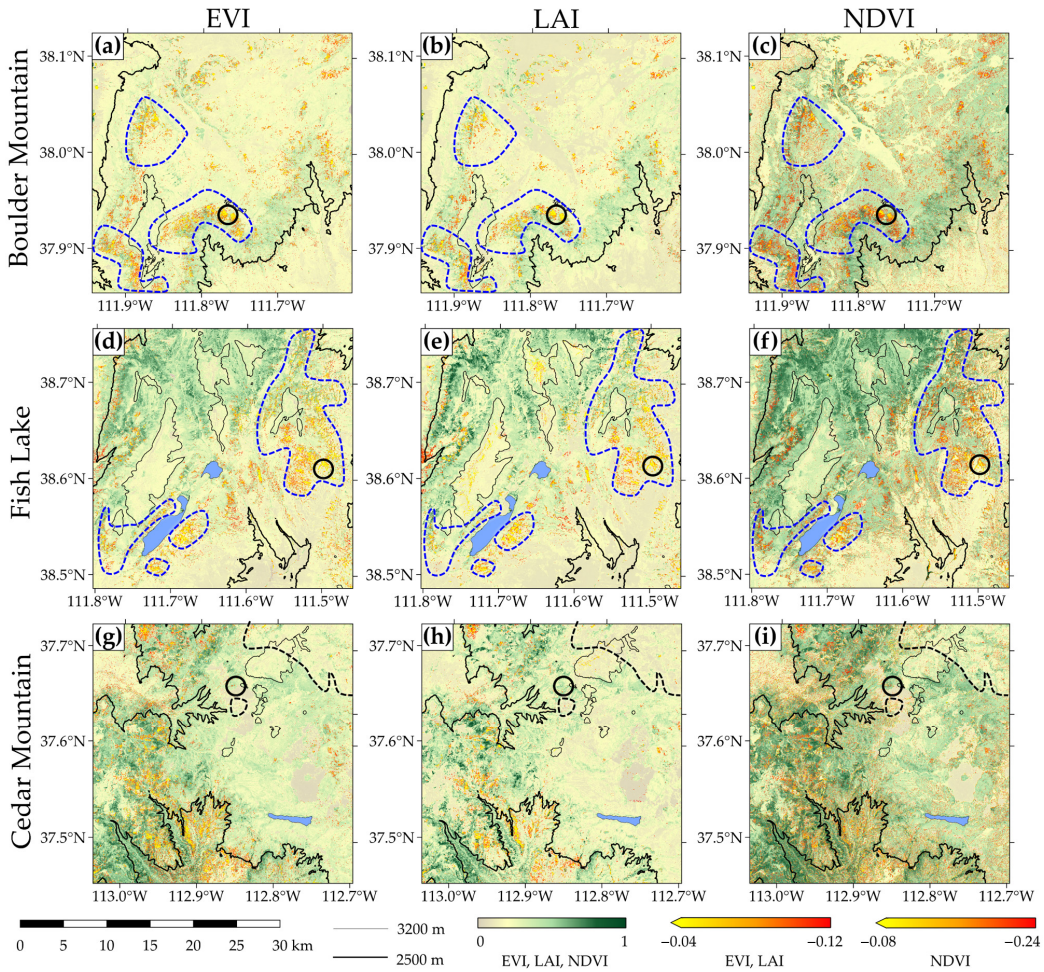

Figure 7. EVI, LAI, and NDVI derived from MSI for 1 July 2020 and the difference in each index from 1 June 2020 for (**a**–**c**) Boulder Mountain, (**d**–**f**) Fish Lake, and (**g**–**i**) Cedar Mountain. Contours delineate elevations at 2500 m (thick black lines) and 3200 m (thin black lines). Black circles indicate locations used for NDVI and GDD regression and time series analyses. Areas outlined in blue indicate areas of freeze damage to aspen and areas outlined in black are fire burn scars.

3.2. Temporal Dynamics of Aspen Responses to the Freeze Event Compared to Average Data

To evaluate the temporal evolution of the NDVI due to freeze damage, we employed a pixel-based analysis for three selected regions: Boulder Mountain, Fish Lake, and Cedar Mountain. Figure 8 provides an illustrative example using MSI imagery, focusing on the Fish Lake site and showcasing our detection method. It emphasizes the grid cell coverage of aspen versus other land cover types for each satellite platform pixel used in the time series. MSI visible color images, using stacked red, green, and blue bands (green band wavelength = 515–605 nm with a 10 m pixel resolution), reveal a reduction in greenness in aspen groves from 1 June 2020 (Figure 8a) to 1 July 2020 (Figure 8b). The area of color change spatially matched the NDVI declines (Figure 8c), where the deciduous forest was detected using 30 m resolution NLCD data (Figure 8d). Across the three sites, MSI pixels covered nearly 100% of aspens. Boulder Mountain and Fish Lake are primarily homogeneous aspen stands, with over 90% of VIIRS and MODIS pixels dominated by aspen at Boulder Mountain and 70–80% for Fish Lake. In contrast, Cedar Mountain is more heterogeneous, with only about 10% of the VIIRS pixels and 20% of the MODIS pixels dominated by aspen, while the rest of the land cover in each consisted of mixed conifer forests and open unforested areas.

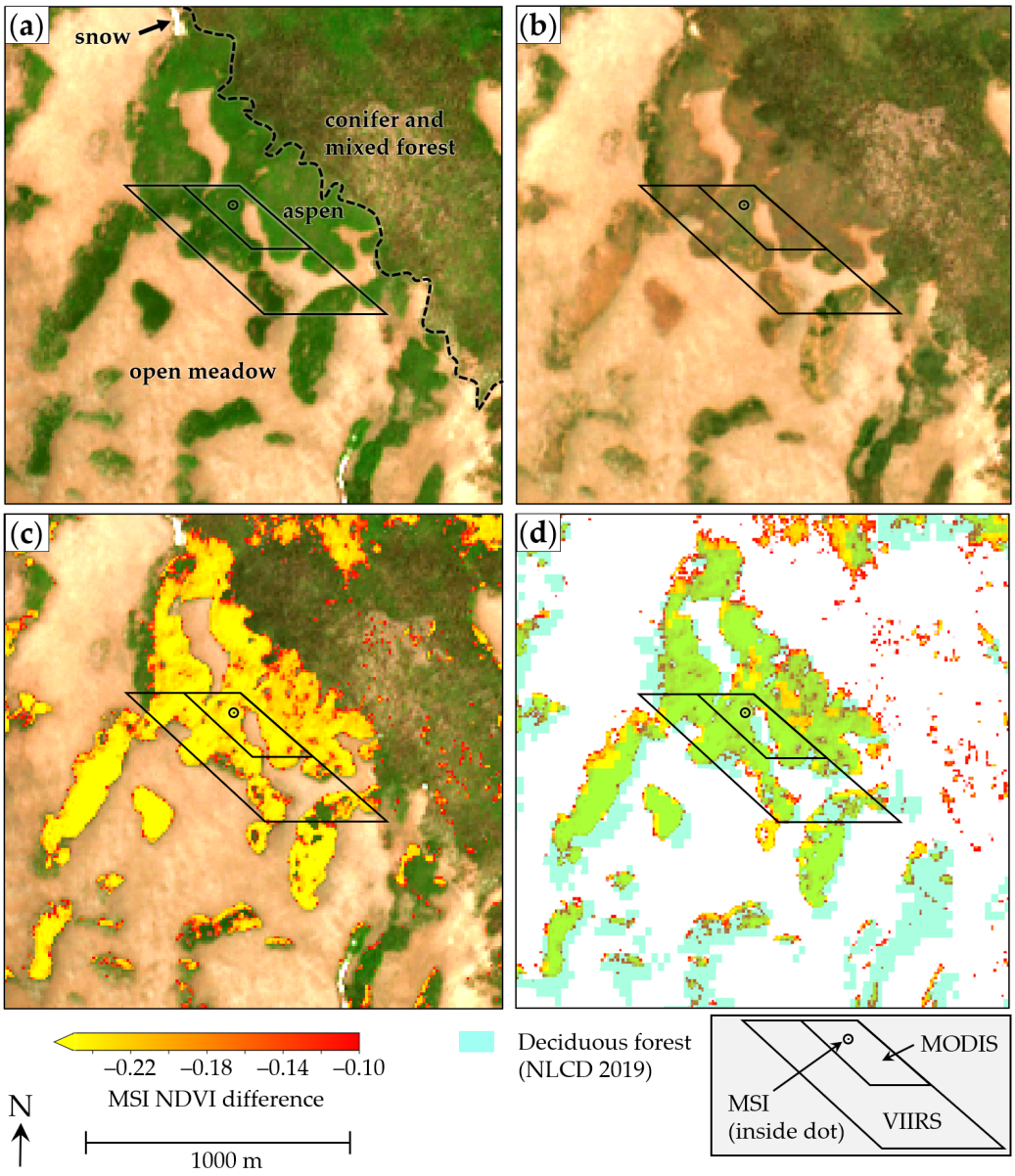

Figure 8. A Sentinel 2 MSI example of visible colors on (**a**) 1 June 2020, with annotations indicating land cover types, (**b**) 1 July 2020, (**c**) 1 June 2020 overlaid with its NDVI difference from 1 July 2020, and (**d**) the same as (**c**), but with NLCD land cover for deciduous forest instead of visible color. Satellite platform grid cell shapes and sizes are indicated at the bottom right. The dotted line indicates the boundary between aspen monoculture and mixed or coniferous forest areas. Maps are centered at 38.614°N, 111.496°W.

Time series results are depicted in Figure 9, which shows the daily NDVI detected for the three selected sites overlaid with the range of one standard deviation estimated from MODIS, denoted by green shades. The spring of 2020 recorded an increase in the NDVI from late April to early June across all platforms at the three selected sites, following the average seasonal cycle denoted by the green shades. However, there were some differences among the sites. From 1 April to 8 June 2020, NDVI values displayed a gradual increase, which occurred earlier than the 2001–2022 average but remained within one standard deviation at Boulder Mountain (Figure 9a). In contrast, at Fish Lake (Figure 9b) and Cedar Mountain (Figure 9c), NDVI values exceeded one standard deviation from late May to early June on all satellite platforms. These results suggest that in 2020, the first flush arrived earlier than under typical conditions.

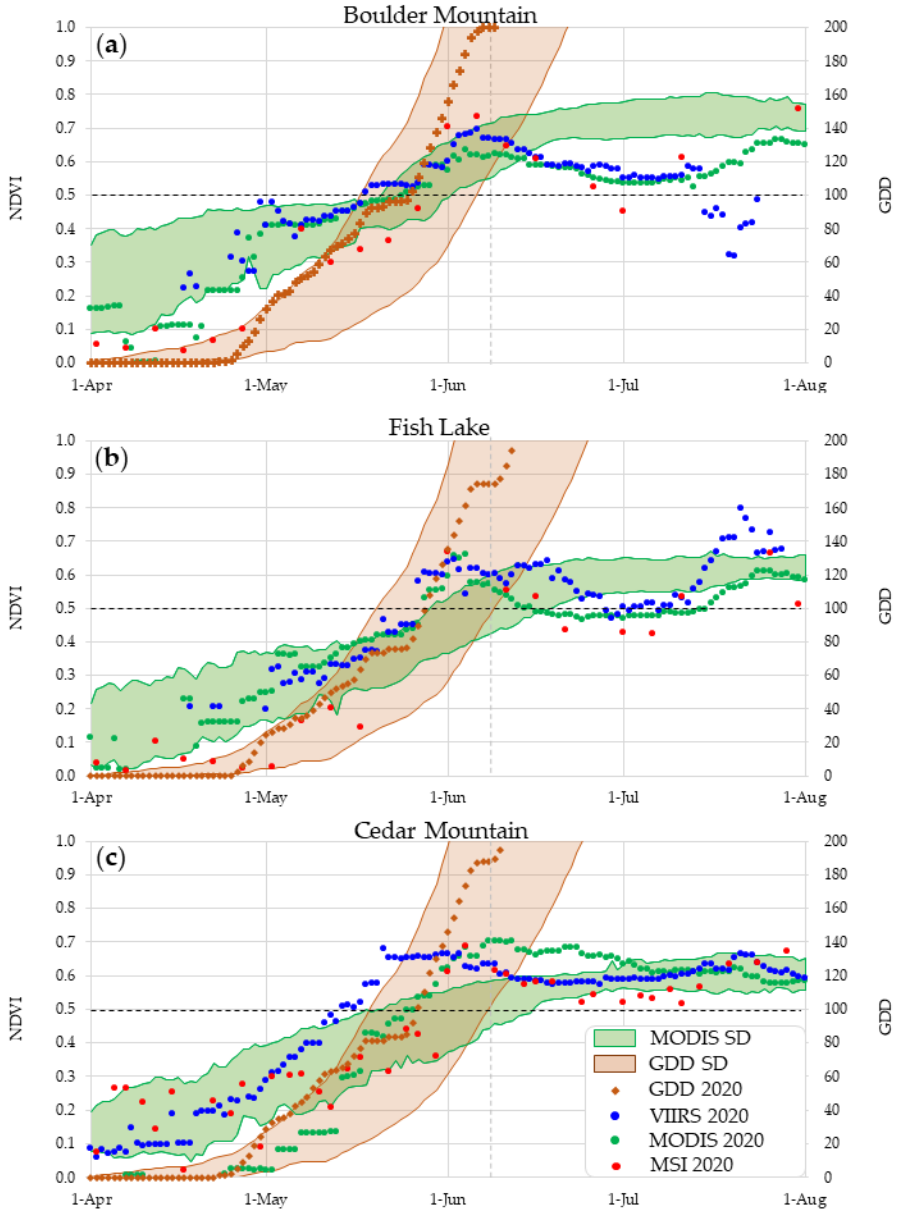

Figure 9. Time series of MODIS, VIIRS, and MSI NDVI values for 2020 (colored symbols), including the MODIS 2001–2022 average ± 1 standard deviation (SD) (shaded green), accumulated growing degree days, including the 2001–2022 average ± 1 standard deviation (shaded brown), and accumulated GDD in 2020 (brown diamonds) for the three subregions of (**a**) Boulder Mountain, (**b**) Fish Lake, and (**c**) Cedar Mountain. The growing degree days are calculated based on a 5 °C baseline. The NDVI at 0.50 is indicated by a horizontal gray dashed line, and the date of the freeze event is depicted as a vertical dashed line.

The temporal evolution of the NDVI coincided with that of the GDD (brown diamonds in Figure 9), highlighted by a steep increase in early May, flattening in mid-late May, and followed by another steep increase afterward. Consistent with this, both the NDVI and GDD exhibited a strong relationship, particularly around the first flush of leaves. An NDVI threshold value of 0.50 (represented by the horizontal black dashed line in Figure 9) generally coincided with a GDD value of 100, marking the intersection of the steepest increase in NDVI associated with the first leaf flush. The simultaneous steep rises in GDD and NDVI across all three sites indicate the consistent influence of accumulated heat on the timing of vegetation greenness, highlighting the direct connection between thermal conditions and vegetation phenology. Nevertheless, the standard deviation of the GDD

was much larger than that of the NDVI, suggesting uncertainty in the pixel-based analysis of NDVI detection.

The time series also captured the timing of the freeze event and the NDVI response afterward. Even though the NDVI reached a local peak in early June, it gradually decreased after the freeze event (vertical gray dashed line in Figure 9). NDVI declines at Boulder Mountain and Fish Lake were consistent between MODIS and MSI. VIIRS exhibited a clear match at Boulder Mountain but was less clear at Fish Lake. At Cedar Mountain, MSI clearly captured the NDVI decline, while the signal was obscured in VIIRS and MODIS data due to the mixed land cover at the site. This NDVI decline continued until around 1 July, with a magnitude of reduction of generally 0.10 to 0.20, followed by a recovery afterward. Declines were most pronounced in the MSI data, with decreases of around 0.20 to 0.30 at all evaluated time series sites, or about a 24 to 38% reduction from pre-freeze peak values. MSI data portrayed consistent NDVI changes across all locations, but did not necessarily capture the absolute peak of the pre-freeze NDVI and the exact freeze event timing, especially at Fish Lake and Cedar Mountain where the last pre-freeze image had cloud cover. MODIS and VIIRS data showed comparable timing of declines immediately post-freeze at Boulder Mountain and Fish Lake, but the temporal evolutions from these platforms did not match MSI at the mixed Cedar Mountain site nor the timing with the other sites. However, the MSI timing matched across the three sites, underscoring the need for a higher resolution to effectively discern dynamics in smaller aspen and mixed land cover settings.

3.3. Confluence of the NDVI and GDD as Metrics to Evaluate the Timing of Freeze Vulnerability Onset

To assess the consistency between the NDVI and GDD, we analyzed the first flush dates estimated from thresholds of the MODIS-based NDVI and GDD for the 2001–2022 period. Figure 10a shows the day of year (DOY) when the MODIS NDVI exceeded 0.50 and when GDD surpassed 100. These DOYs provide a rough estimate of the first flush dates derived from NDVI and GDD. Consistent with the time-series analysis, the estimated first flush dates showed strong positive correlations, with R values of 0.82 at Boulder Mountain, 0.81 at Fish Lake, and 0.74 at Cedar Mountain (Figure 10a). This high correlation supported our approach for estimating the first flush date from the thresholds of NDVI or GDD. Outliers in the NDVI-based estimate that exceeded DOY 170 at Fish Lake and Cedar Mountain while the DOY at GDD > 100 was under 150 originated from an exceptionally deep snowpack concurrent with near-average spring temperatures. The average dates for the initial flush, identified by an NDVI greater than 0.50, were DOY 149 for Boulder Mountain, DOY 157 for Fish Lake, and DOY 155 for Cedar Mountain. Conversely, the first flush, indicated by a GDD surpassing 100, occurred on DOY 151 for Boulder Mountain, DOY 150 for Fish Lake, and DOY 149 for Cedar Mountain. Since DOY 150 corresponds to 28 May in non-leap years, the aspen's first flush at this elevation typically occurs in late May to early June.

Whereas the GDD threshold of 100 provides the estimated first flush date, there are some uncertainties associated with this GDD-based threshold. Figure 10b shows the GDD value on the date when the MODIS-based NDVI exceeded 0.50. During the 2001–2022 record, GDD values mostly fell within the 60–160 range, affirming the GDD threshold of 100. The average GDD values varied across the sites: 91 at Boulder Mountain, 112 at Cedar Mountain, and 136 at Fish Lake. The fluctuation in these GDD values depends on the quality of daily temperature data, the elevation of weather stations, and the DOY estimated from the MODIS-based NDVI. In particular, daily temperatures are colder at higher elevations, which is the main factor contributing to smaller GDD values at Boulder Mountain. Nevertheless, these results suggest that the GDD threshold of 100 is a reasonable assumption for estimating the first flush date from weather station data. Further discussion about the uncertainty of the estimated first flush date is described below.

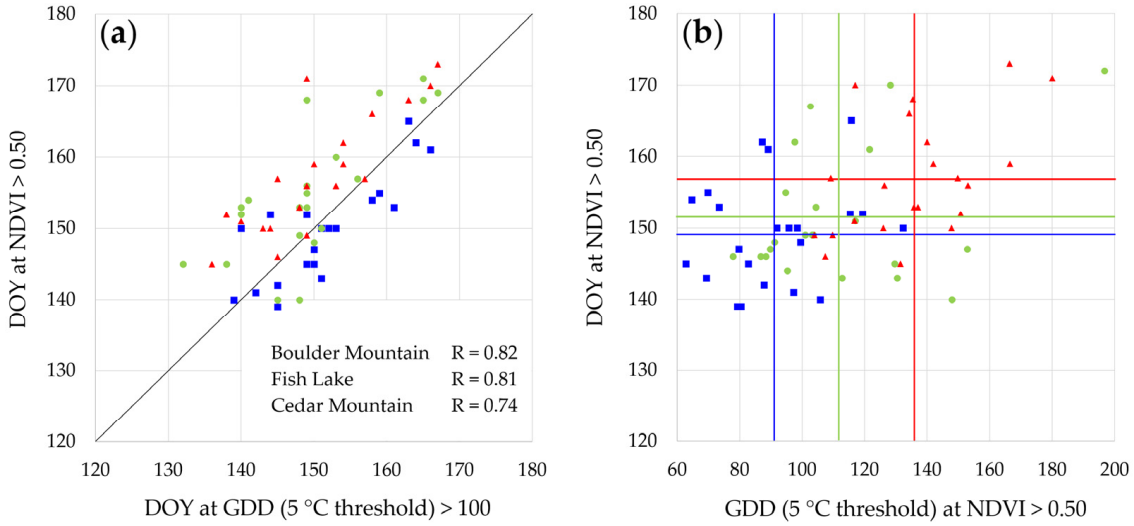

Figure 10. Scatterplots of the three referenced locations in Figure 3, with (**a**) the DOY at GDD exceeding 100 (x-axis) with DOY when the MODIS NDVI exceeds 0.50 (y-axis), and (**b**) GDD value when the MODIS NDVI exceeds 0.50 (x-axis) with the DOY when the MODIS NDVI exceeds 0.50 (y-axis) and their respective average values (lines) in each dimension, with blue being Boulder Mountain, red being Fish Lake, and green being Cedar Mountain. Pearson's correlation coefficient (R) values are indicated in (**a**).

4. Discussion

4.1. Effective Detection and Requisite Spatial Resolution

Our study underscores the effectiveness of using medium- and high-resolution remote sensing, in conjunction with local temperature data, to assess the timing of the spring leaf flush, subsequent freeze vulnerability, and the impact of freeze-induced damage on aspen. The strategic use of multiple satellite platforms exploits the strengths of each, including daily temporal resolution from MODIS and VIIRS and the high spatial resolution from MSI, to cross-validate and confirm the timing and spatial extent of the first flush, freeze damage, and second flush. Furthermore, it allows an analysis at smaller landscape and microclimate scales. Our findings suggest that VIIRS and MODIS are more effective for detecting extensive aspen damage over larger, homogeneous stands, while MSI provides superior detection capabilities in smaller, more heterogeneous stands.

We employed two spatial representations of freeze damage—the median deviation and change detection methods—across three remotely sensed datasets. While the median deviation method effectively identified areas of damage or defoliation, variations arose due to differences in spatial resolution. High-resolution MSI data clearly outperformed MODIS and VIIRS, offering more precise spatial detail, while MODIS was successful in identifying freeze damage in larger aspen stands, although results were less distinct in VIIRS data. Previous studies have reached similar conclusions but focused on different species and methods. For example, one study combined MODIS NDVI data with downscaled reanalysis temperatures to identify freeze damage in European beech forests [80]. They highlighted that higher-resolution imagery from platforms like Landsat 7, 8, and Sentinel 2 could mitigate the limitations of MODIS's coarser resolution. Another study focused on the Iberian Peninsula and used both MODIS and MSI, along with Landsat data, to detect defoliation in beech forests [38]. However, their approach relied on a computationally intensive machine learning model, limiting the number of pixels analyzed, and required prior knowledge of damage to select high-resolution data for training. In contrast, our study presents a simpler and more efficient approach by directly using high-resolution MSI data to detect freeze-induced defoliation in aspen forests without the need for machine learning models or preselected areas. This straightforward method not only improves efficiency but also has practical implications for forest management. Providing a reliable

and scalable means of monitoring freeze damage across large areas allows forest managers to identify vulnerable stands more quickly and accurately, enabling more proactive and informed decision-making for the conservation and management of aspen forests.

Our findings using NDVI were corroborated with other vegetation indices, LAI and EVI, validating the simpler and established NDVI as a metric for determining freeze damage and recovery in aspen. Since NDVI is the least expensive of the vegetation indices in terms of computation and data storage, and with data being available within a day of acquisition, this makes it ideal for the rapid detection of freeze damage. Furthermore, the methods are easily adaptable by managers to quantify the impacts of freeze events. Finally, our validation of the GDD thresholds presents a valuable tool in assessing past, present, and future trends in climate change-driven shifts in the first flush and their potential impacts on the vulnerability of aspen.

4.2. Temporal Dynamics

Time series data demonstrate the advantages of a high temporal resolution, as well as the limitations posed by coarser resolutions. For instance, the sharp NDVI decline immediately following the freeze event, observed in the daily data and even in the five-day time step of MSI, helped confirm the impact of the freeze event through rapid physiological responses in aspen canopies [10,46]. However, coarser resolution data struggled to represent highly varied landscapes, such as the heterogeneous mixed forest at the Cedar Mountain site. The declines and the absence of a July NDVI rebound or second flush in the coarser VIIRS and MODIS data suggest summertime drying in the mixed forest environment [81]. In contrast, the MSI data, which captured the small aspen grove (see Figure 2) at Cedar Mountain's UFDP [82], indicated a sharp post-freeze NDVI decline followed by a second flush [2,9,17], similar to what was observed at the more homogeneous Boulder Mountain and Fish Lake sites. At these latter sites, daily data from VIIRS, and especially MODIS, complemented MSI by filling gaps and backing up missing data. Additionally, the inclusion of 22 years of daily MODIS data, 11 years of VIIRS data, and 6 years of MSI data build more robust statistics against which to compare a reference year, whereas previous studies relied only on 16-day MODIS periods for aspen analysis [2,4].

4.3. Correlation with the Growing Degree Model

Our study also highlights the consistency of detecting the first flush using satellite data alongside elevation-adjusted weather station data to determine when aspen canopies become vulnerable to freeze. The adjustment of temperature and resultant GDD values based on elevation—centered in the aspen areas of southern Utah—produced more representative values. However, some uncertainty may have been introduced due to the approximate 700 m elevation range for the majority of aspen in the region. Slope and aspect also play crucial roles in aspen phenology, with south-facing slopes generally flushing earlier and having a longer growing season due to locally increased temperatures and earlier spring snowmelt [6,45]. This pattern is evident when comparing the NDVI-based first flush with slope observations derived from SRTM elevation data at the time series sites. For instance, at Boulder Mountain, where the site is located on a steep south-facing slope, the NDVI-based first flush occurred seven days earlier compared to the shallow southwest-facing slope at Fish Lake, and five days earlier than at the Cedar Mountain site, which is on a shallow west-facing slope.

The correlation between the estimated DOYs from GDD and NDVI thresholds at all three sites was strong, as observed in other studies, despite uncertainties brought by topography. Another study similarly found high correlations between the GDD and vegetation indices in central Canada [51]. They used a GDD threshold of 5 °C and identified a value of 120 to mark the first flush. Additionally, they reported NDVI-based first greening at 0.42 but used 0.60 as the threshold for the first flush in their regression analysis, finding an average DOY of 140 compared to their GDD first flush at DOY 13, approximately two weeks earlier than our results. Their time series analysis supports these figures for central Canada

at a 600 m elevation, while our results validated the NDVI and GDD thresholds of 0.50 and 100, respectively, as markers for the onset of aspen flush in southern Utah at around 3000 m. Differences clearly arise from local climate and elevation. Other research has found similar threshold values for aspen, though with regional variation [32,49]. These DOY estimates could serve as predictive metrics for the first flush, offering a valuable tool for assessing past events and informing future research and monitoring of montane aspen ecosystems.

4.4. Ruling Out Other Defoliators

In concluding that the NDVI decline observed in the summer of 2020 was primarily due to freeze damage, we considered and ruled out other causes of defoliation, such as pests, diseases, drought, and wildfires. This was facilitated by the high temporal resolution employed in the study. In Utah, the western tent caterpillar, large aspen tortrix, and aspen two-leaf tier are known as aspen defoliators [11]. Their damage progresses spatially over time and can result in multi-year outbreaks [2,43,44], as opposed to the NDVI of freeze-damaged areas simultaneously declining after the freeze date. Marssonina Leaf Blight (*Drepanopeziza*), another aspen defoliator in Utah, typically causes progressive leaf loss throughout the summer, also with spatial progression, and is occasionally followed by a late-summer second flush [13,83]. Drought influences plant phenology differently, leading to gradual and nonuniform defoliation without a subsequent flush [4]. These findings support the conclusion that in montane aspen stands of southern Utah the widespread NDVI decline and its recovery in early summer 2020 were primarily attributed to freeze-induced defoliation rather than other common defoliating agents.

5. Conclusions

Combining medium- and high-resolution remote sensing with local temperature data provides a detailed and accurate representation of growing season freeze-induced damage to aspen stands, their spring phenology, and freeze vulnerability. Our spatial analysis, employing multiple satellite platforms, highlights the crucial role of spatial resolution in assessing the extent and intensity of freeze-induced aspen defoliation. The 10 m resolution MSI data proved significantly more accurate and precise spatially than VIIRS and MODIS data. Nevertheless, for larger homogeneous stands, the near-daily temporal resolution of MODIS and VIIRS was sufficient to capture aspen response and recovery dynamics following freeze events. Conversely, the five-day time step of MSI data makes the time series analysis more susceptible to missing data from cloud cover, as we found with Landsat OLI. However, given adequate clear-sky observations, it can successfully capture these dynamics and for much smaller aspen stands. Furthermore, our NDVI and GDD thresholds for predicting spring flush timing—derived from weather station and satellite data—demonstrate a strong correlation, confirming GDD as a reliable indicator for the onset of aspen flush in Utah. Despite the inherent challenges in satellite detection and environmental complexity, our study addresses these systematically, providing a comprehensive analysis of the 2020 freeze event's impact on aspen-dominated forests.

This work underscores the significance of multidisciplinary methods, demonstrating the essential integration of meteorological, remote sensing, and field observations to better understand climate effects on canopy dynamics. Beyond advancing knowledge of the vegetation response to extreme weather events, this study illuminates broader implications for forest dynamics and ecosystem resilience against the backdrop of changing climate conditions. The methods introduced here for detecting aspen defoliation using multispectral data hold promise for both academic research and practical forest management, particularly for monitoring forest health and vulnerability in remote regions with limited human access. These methods are applicable not only to aspen but also to other species and agricultural interests. Additionally, the methods developed for estimating canopy flush dates have diverse applications, including differentiating freeze-related damage from other defoliators; assessments of past occurrences, current vulnerabilities, the potential role in aspen's decline; and predictions of future climatic threats. Finally, the methods presented

in this study can be further enhanced by leveraging other high-resolution satellite data, such as the pairing of Landsat 8 and 9, as well as data from Planet Labs Dove satellites.

Author Contributions: Conceptualization, T.E.W. and Y.C.; methodology, T.E.W. and Y.C.; software, T.E.W. and Y.C.; validation, T.E.W. and Y.C.; formal analysis, T.E.W.; investigation, T.E.W.; resources, T.E.W. and Y.C.; data curation, T.E.W.; writing—original draft preparation, T.E.W.; writing—review and editing, T.E.W., Y.C., J.D.B., and J.A.L.; visualization, T.E.W.; supervision, Y.C.; project administration, T.E.W. and Y.C.; funding acquisition, Y.C. All authors have read and agreed to the published version of the manuscript.

Funding: Y.C. is supported by the Utah Agricultural Experiment Station, Utah State University (approved as journal paper #9820), the Cedar Mountain Initiative, U.S. Geological Survey and Utah Center for Water Resources Research for the 104b grant (G21AP10623-04), the U.S. Department of Interior, Bureau of Reclamation (R22AP00220 and R24AP00321), the Strategic Environmental Research and Development Program (RC20-3056), and a US Department of Energy grant (DESC0016605).

Data Availability Statement: Land cover data were obtained at https://s3-us-west-2.amazonaws.com/mrlc/nlcd_2019_land_cover_l48_20210604.zip (accessed on 2 September 2022). GHCN station data were obtained through the Utah Climate Center at Utah State University at https://climate.usu.edu/swco/ (accessed on 18 April 2023). Shuttle Radar Topography Mission (SRTM) elevation data were obtained at https://earthexplorer.usgs.gov/ (accessed on 2 September 2022). Sentinel 2 data were obtained at https://console.cloud.google.com/storage/browser/gcp-public-data-sentinel-2/ (accessed on 8 January 2023). Sentinel 2 LAI data were calculated and obtained from https://custom-scripts.sentinel-hub.com/custom-scripts/sentinel-2/lai/ (accessed on 9 January 2023). VIIRS and MODIS data were obtained from https://appeears.earthdatacloud.nasa.gov/ (accessed on 8 January 2023). The raw data supporting the conclusions of this article will be made available by the authors on request.

Conflicts of Interest: The authors declare no conflicts of interest.

References

1. Ding, C.; Schreiber, S.G.; Roberts, D.R.; Hamann, A.; Brouard, J.S. Post-Glacial Biogeography of Trembling Aspen Inferred from Habitat Models and Genetic Variance in Quantitative Traits. *Sci. Rep.* **2017**, *7*, 4672. [CrossRef] [PubMed]
2. Currit, N.; St. Clair, S.B. Assessing the Impact of Extreme Climatic Events Aspen Defoliation Using MODIS Imagery. *Geocarto Int.* **2010**, *25*, 133–147. [CrossRef]
3. Laganière, J.; Boča, A.; Van Miegroet, H.; Paré, D. A Tree Species Effect on Soil That Is Consistent across the Species' Range: The Case of Aspen and Soil Carbon in North America. *Forests* **2017**, *8*, 113. [CrossRef]
4. Meier, G.A.; Brown, J.F.; Evelsizer, R.J.; Vogelmann, J.E. Phenology and Climate Relationships in Aspen (*Populus Tremuloides Michx.*) Forest and Woodland Communities of Southwestern Colorado. *Ecol. Indic.* **2015**, *48*, 189–197. [CrossRef]
5. St. Clair, S.B.; Guyon, J.; Donaldson, J. Quaking Aspen's Current and Future Status in Western North America: The Role of Succession, Climate, Biotic Agents and Its Clonal Nature. In *Progress in Botany 71*; Springer: Berlin/Heidelberg, Germany, 2010; Volume 71, pp. 371–400. [CrossRef]
6. Worrall, J.J.; Egeland, L.; Eager, T.; Mask, R.A.; Johnson, E.W.; Kemp, P.A.; Shepperd, W.D. Rapid Mortality of *Populus Tremuloides* in Southwestern Colorado, USA. *For. Ecol. Manag.* **2008**, *255*, 686–696. [CrossRef]
7. Worrall, J.J.; Rehfeldt, G.E.; Hamann, A.; Hogg, E.H.; Marchetti, S.B.; Michaelian, M.; Gray, L.K. Recent Declines of *Populus Tremuloides* in North America Linked to Climate. *For. Ecol. Manag.* **2013**, *299*, 35–51. [CrossRef]
8. Baker, F.S. Aspen in the Central Rocky Mountain Region. *USDA* **1925**, *1291*, 47. [CrossRef]
9. St. Clair, S.B.; Monson, S.D.; Smith, E.A.; Cahill, D.G.; Calder, W.J. Altered Leaf Morphology, Leaf Resource Dilution and Defense Chemistry Induction in Frost-Defoliated Aspen (*Populus Tremuloides*). *Tree Physiol.* **2009**, *29*, 1259–1268. [CrossRef]
10. Rubert-Nason, K.F.; Couture, J.J.; Gryzmala, E.A.; Townsend, P.A.; Lindroth, R.L. Vernal Freeze Damage and Genetic Variation Alter Tree Growth, Chemistry, and Insect Interactions. *Plant Cell Environ.* **2017**, *40*, 2743–2753. [CrossRef]
11. Guyon, J.; Hoffman, J. *Survey of Aspen Disease in the Intermountain Region (R4-OFO-Report 11-01)*; USDA Forest Service: Ogden, UT, USA, 2011; pp. 19p. Available online: https://digitalcommons.usu.edu/cgi/viewcontent.cgi?article=8039&context=aspen_bib&httpsredir=1&referer= (accessed on 7 January 2024).
12. Hogg, E.H.; Brandt, J.P.; Michaelian, M. Impacts of a Regional Drought on the Productivity, Dieback, and Biomass of Western Canadian Aspen Forests. *Can. J. For. Res.* **2008**, *38*, 1373–1384. [CrossRef]
13. Call, A.C.; Clair, S.B.S. Outbreak of Drepanopeziza Fungus in Aspen Forests and Variation in Stand Susceptibility: Leaf Functional Traits, Compensatory Growth and Phenology. *Tree Physiol.* **2017**, *37*, 1198–1207. [CrossRef]
14. Marchetti, S.B.; Worrall, J.J.; Eager, T. Secondary Insects and Diseases Contribute to Sudden Aspen Decline in Southwestern Colorado, USA. *Can. J. For. Res.* **2011**, *41*, 2315–2325. [CrossRef]

15. Rogers, P.C. *Guide to quaking aspen ecology and management with emphasis on Bureau of Land Management Lands in the Western United States*; Western Aspen Alliance: Logan, UT, USA, 2017; pp. 98p. Available online: https://digitalcommons.usu.edu/aspen_bib/7606/ (accessed on 7 January 2024).
16. Michaelian, M.; Hogg, E.H.; Hall, R.J.; Arsenault, E. Massive Mortality of Aspen Following Severe Drought along the Southern Edge of the Canadian Boreal Forest. *Glob. Chang. Biol.* **2011**, *17*, 2084–2094. [CrossRef]
17. Birch, J.D.; Chikamoto, Y.; DeRose, R.J.; Manvailer, V.; Hogg, E.H.; Karst, J.; Love, D.M.; Lutz, J.A. Frost-Associated Defoliation in Populus Tremuloides Causes Repeated Growth Reductions Over 185 Years. *Ecosystems* **2023**, *26*, 843–859. [CrossRef]
18. Yamaguchi, D.K.; Filion, L.; Savage, M. Relationship of Temperature and Light Ring Formation at Subarctic Treeline and Implications for Climate Reconstruction. *Quat. Res.* **1993**, *39*, 256–262. [CrossRef]
19. Szeicz, J.M.; MacDonald, G.M. A 930-Year Ring-Width Chronology from Moisture-Sensitive White Spruce (*Picea Glauca Moench*) in Northwestern Canada. *Holocene* **1996**, *6*, 345–351. [CrossRef]
20. Wang, L.; Payette, S.; Bégin, Y. A Quantitative Definition of Light Rings in Black Spruce (*Picea Mariana*) at the Arctic Treeline in Northern Québec, Canada. *Arct. Antarct. Alp. Res.* **2000**, *32*, 324–330. [CrossRef]
21. Filion, L.; Cournoyer, L. Variation in Wood Structure of Eastern Larch Defoliated by the Larch Sawfly in Subarctic Quebec, Canada. *Can. J. For. Res.* **1995**, *25*, 1263–1268. [CrossRef]
22. Girardin, M.P.; Tardif, J.; Bergeron, Y. Radial Growth Analysis of Larix Laricina from the Lake Deparquet Area, Québec, in Relation to Climate and Larch Sawfly Outbreaks. *Ecoscience* **2001**, *8*, 127–138. [CrossRef]
23. Kulman, H.M.; Hodson, A.C.; Duncan, D.P. Distribution and Effects of Jack-Pine Budworm Defoliation. *For. Sci.* **1963**, *9*, 146–157. [CrossRef]
24. Volney, W.J.A.; Mallett, K.I. Light Rings and the Age of Jack Pine Trees. *Can. J. For. Res.* **1992**, *22*, 2011–2013. [CrossRef]
25. Liang, C.; Filion, L.; Cournoyer, L. Wood Structure of Biotically and Climatically Induced Light Rings in Eastern Larch (*Larix Laricina*). *Can. J. For. Res.* **1997**, *27*, 1538–1547. [CrossRef]
26. Hogg, E.H.; Hart, M.; Lieffers, V.J. White Tree Rings Formed in Trembling Aspen Saplings Following Experimental Defoliation. *Can. J. For. Res.* **2002**, *32*, 1929–1934. [CrossRef]
27. Kross, A.; Fernandes, R.; Seaquist, J.; Beaubien, E. The Effect of the Temporal Resolution of NDVI Data on Season Onset Dates and Trends across Canadian Broadleaf Forests. *Remote Sens. Environ.* **2011**, *115*, 1564–1575. [CrossRef]
28. Reed, B.C. Trend Analysis of Time-Series Phenology of North America Derived from Satellite Data. *GIsci Remote Sens.* **2006**, *43*, 24–38. [CrossRef]
29. Neigh, C.S.R.; Tucker, C.J.; Townshend, J.R.G. Synchronous NDVI and Surface Air Temperature Trends in Newfoundland: 1982 to 2003. *Int. J. Remote Sens.* **2007**, *28*, 2581–2598. [CrossRef]
30. Huemmrich, K.F.; Black, T.A.; Jarvis, P.G.; McCaughey, J.H.; Hall, F.G. High Temporal Resolution NDVI Phenology from Micrometeorological Radiation Sensors. *J. Geophys. Res. Atmos.* **1999**, *104*, 27935–27944. [CrossRef]
31. Huete, A.; Didan, K.; Miura, T.; Rodriguez, E.P.; Gao, X.; Ferreira, L.G. Overview of the Radiometric and Biosphysical Performance of the MODIS Vegetation Indices. *Remote Sens. Environ.* **2002**, *83*, 195–213. [CrossRef]
32. Donnelly, A.; Yu, R.; Caffarra, A.; Hanes, J.; Liang, L.; Desai, A.R.; Liu, L.; Schwartz, M.D. Interspecific and Interannual Variation in the Duration of Spring Phenophases in a Northern Mixed Forest. *Agric. For. Meteorol.* **2017**, *243*, 55–67. [CrossRef]
33. McCloskey, L.; Sams, B.; Harris, J.L.; Salie, M.; Striegler, R.K.; Sanchez, L.; Dokoozlian, N. 120. Relationships between Freeze Damaged Vines and Imagery from Satellites and Unmanned Aerial Vehicles in California Vineyards. In *Precision Agriculture '23*; Wageningen Academic Publishers: Washington, DC, USA, 2023; pp. 120–955. ISBN 978-90-8686-393-8.
34. Cogato, A.; Meggio, F.; Collins, C.; Marinello, F. Medium-Resolution Multispectral Data from Sentinel-2 to Assess the Damage and the Recovery Time of Late Frost on Vineyards. *Remote Sens.* **2020**, *12*, 1896. [CrossRef]
35. Wegler, M.; Kuenzer, C. Potential of Earth Observation to Assess the Impact of Climate Change and Extreme Weather Events in Temperate Forests—A Review. *Remote Sens.* **2024**, *16*, 2224. [CrossRef]
36. Decuyper, M.; Chávez, R.O.; Čufar, K.; Estay, S.A.; Clevers, J.G.P.W.; Prislan, P.; Gričar, J.; Črepinšek, Z.; Merela, M.; de Luis, M.; et al. Spatio-Temporal Assessment of Beech Growth in Relation to Climate Extremes in Slovenia – An Integrated Approach Using Remote Sensing and Tree-Ring Data. *Agric. For. Meteorol.* **2020**, *287*, 107925. [CrossRef]
37. Molnár, T.; Király, G. Forest Disturbance Monitoring Using Cloud-Based Sentinel-2 Satellite Imagery and Machine Learning. *J. Imaging* **2024**, *10*, 14. [CrossRef]
38. Olano, J.M.; García-Cervigón, A.I.; Sangüesa-Barreda, G.; Rozas, V.; Muñoz-Garachana, D.; García-Hidalgo, M.; García-Pedrero, Á. Satellite Data and Machine Learning Reveal the Incidence of Late Frost Defoliations on Iberian Beech Forests. *Ecol. Appl.* **2021**, *31*, 1–11. [CrossRef] [PubMed]
39. She, B.; Huang, J.F.; Zhang, D.Y.; Huang, L.S. Assessing and Characterizing Oilseed Rape Freezing Injury Based on MODIS and MERIS Data. *Int. J. Agric. Biol. Eng.* **2017**, *10*, 143–157. [CrossRef]
40. Feng, M.-C.; Yang, W.-D.; Cao, L.-L.; Ding, G.-W. Monitoring Winter Wheat Freeze Injury Using Multi-Temporal MODIS Data. *Agric. Sci. China* **2009**, *8*, 1053–1062. [CrossRef]
41. Stephens, J.J.; Black, T.A.; Jassal, R.S.; Nesic, Z.; Grant, N.J.; Barr, A.G.; Helgason, W.D.; Richardson, A.D.; Johnson, M.S.; Christen, A. Effects of Forest Tent Caterpillar Defoliation on Carbon and Water Fluxes in a Boreal Aspen Stand. *Agric. For. Meteorol.* **2018**, *253–254*, 176–189. [CrossRef]

42. Thomas, S.J.; Deschamps, A.; Landry, R.; Van Der Sanden, J.J.; Hall, R.J. Mapping Insect Defoliation Using Multi-Temporal Landsat Data. In Proceedings of the American Society for Photogrammetry and Remote Sensing—28th Canadian Symposium on Remote Sensing and ASPRS Fall Specialty Conference 2007, Ottawa, ON, Canada, 28 October–1 November 2007; pp. 248–257.
43. Hall, R.J.; Castilla, G.; White, J.C.; Cooke, B.J.; Skakun, R.S. Remote Sensing of Forest Pest Damage: A Review and Lessons Learned from a Canadian Perspective. *Can. Entomol.* **2016**, *148*, S296–S356. [CrossRef]
44. Hall, R.; Arsenault, E.; Skakun, R. Remotely Sensed Data in the Mapping of Insect Defoliation. *Underst. For. Disturb. Spat. Pattern* **2006**, 85–111. [CrossRef]
45. Blonder, B.W.; Brodrick, P.G.; Chadwick, K.D.; Carroll, E.; Cruz-de Hoyos, R.M.; Expósito-Alonso, M.; Hateley, S.; Moon, M.; Ray, C.A.; Tran, H.; et al. Climate Lags and Genetics Determine Phenology in Quaking Aspen (*Populus tremuloides*). *New Phytol.* **2023**, *238*, 2313–2328. [CrossRef]
46. Man, R.; Lu, P.; Colombo, S.; Li, J.; Dang, Q. Photosynthetic and Morphological Responses of White Birch, Balsam Poplar, and Trembling Aspen to Freezing and Artificial Defoliation. *Botany* **2013**, *91*, 343–348. [CrossRef]
47. Hogg, E.H.; Brandt, J.P.; Kochtubajda, B. Growth and Dieback of Aspen Forests in Northwestern Alberta, Canada, in Relation to Climate and Insects. *Can. J. For. Res.* **2002**, *32*, 823–832. [CrossRef]
48. Hogg, E.H. Simulation of Interannual Responses of Trembling Aspen Stands to Climatic Variation and Insect Defoliation in Western Canada. *Ecol. Modell.* **1999**, *114*, 175–193. [CrossRef]
49. Li, H.; Wang, X.; Hamann, A. Genetic Adaptation of Aspen (*Populus tremuloides*) Populations to Spring Risk Environments: A Novel Remote Sensing Approach. *Can. J. For. Res.* **2010**, *40*, 2082–2090. [CrossRef]
50. Springer, K.R.; Wang, R.; Gamon, J.A. Parallel Seasonal Patterns of Photosynthesis, Fluorescence, and Reflectance Indices in Boreal Trees. *Remote Sens.* **2017**, *9*, 691. [CrossRef]
51. Barr, A.; Black, T.A.; McCaughey, H. *Climatic and Phenological Controls of the Carbon and Energy Balances of Three Contrasting Boreal Forest Ecosystems in Western Canada BT—Phenology of Ecosystem Processes: Applications in Global Change Research*; Noormets, A., Ed.; Springer: New York, NY, USA, 2009; pp. 3–34. ISBN 978-1-4419-0026-5.
52. Rogers, P.C.; Leffler, A.J.; Ryel, R.J. Landscape Assessment of a Stable Aspen Community in Southern Utah, USA. *For. Ecol. Manage* **2010**, *259*, 487–495. [CrossRef]
53. Oukrop, C.M.; Evans, D.M.; Bartos, D.L.; Ramsey, R.D.; Ryel, R.J. *Moderate-Scale Mapping Methods of Aspen Stand Types: A Case Study for Cedar Mountain in Southern Utah*; United States Department of Agriculture: New York, NY, USA, 2011; pp. 1–18. [CrossRef]
54. Tao, J.; Man, R.; Dang, Q.L. Earlier and more variable spring phenology projected for eastern Canadian boreal and temperate forests with climate warming. *Trees, Forests and People.* **2021**, *6*, 100127. [CrossRef]
55. Menne, M.J.; Durre, I.; Korzeniewski, B.; McNeal, S.; Thomas, K.; Yin, X.; Anthony, S.; Ray, R.; Vose, R.S.; Gleason, B.E. Global Historical Climatology Network—Daily (GHCN-Daily), Version 3—Subset US Collection. Available online: https://climate.usu.edu/swco/ (accessed on 9 January 2023).
56. Hersbach, H.; Bell, B.; Berrisford, P.; Biavati, G.; Horányi, A.; Muñoz Sabater, J.; Nicolas, J.; Peubey, C.; Radu, R.; Rozum, I.; et al. ERA5 Hourly Data on Pressure Levels from 1940 to Present. Available online: https://cds.climate.copernicus.eu/cdsapp#!/dataset/reanalysis-era5-pressure-levels?tab=overview (accessed on 9 March 2023).
57. Vermote, E. MODIS/Terra Surface Reflectance 8-Day L3 Global 250m SIN Grid V061. Available online: https://appeears.earthdatacloud.nasa.gov/ (accessed on 8 January 2023).
58. Vermote, E.; Wolfe, R. MOD09GQ MODIS/Terra Surface Reflectance Daily L2G Global 250m SIN Grid V006 [Data Set]. Available online: https://appeears.earthdatacloud.nasa.gov/ (accessed on 7 January 2023).
59. Vargas, M.; Miura, T.; Shabanov, N.; Kato, A. An Initial Assessment of Suomi NPP VIIRS Vegetation Index EDR. *J. Geophys. Res. Atmos.* **2013**, *118*, 12301–12316. [CrossRef]
60. Skakun, S.; Justice, C.O.; Vermote, E.; Roger, J.C. Transitioning from MODIS to VIIRS: An Analysis of Inter-Consistency of NDVI Data Sets for Agricultural Monitoring. *Int. J. Remote Sens.* **2018**, *39*, 971–992. [CrossRef]
61. Agency, E.S. Copernicus Sentinel-2 (Processed by ESA) MSI Level-2A BOA Reflectance Product. Collection 1. Available online: https://console.cloud.google.com/storage/browser/gcp-public-data-sentinel-2 (accessed on 8 January 2023).
62. Vermote, E.R.W. *MODIS/Terra Surface Reflectance Daily L2G Global 250m SIN Grid V061*; ASA EOSDIS Land Processes DAAC: Missoula, MT, USA, 2021.
63. Liu, Y.; Wang, Z.; Sun, Q.; Erb, A.M.; Li, Z.; Schaaf, C.B.; Zhang, X.; Román, M.O.; Scott, R.L.; Zhang, Q.; et al. Evaluation of the VIIRS BRDF, Albedo and NBAR Products Suite and an Assessment of Continuity with the Long Term MODIS Record. *Remote Sens. Environ.* **2017**, *201*, 256–274. [CrossRef]
64. Li, Z.; Erb, A.; Sun, Q.; Liu, Y.; Shuai, Y.; Wang, Z.; Boucher, P.; Schaaf, C. Preliminary Assessment of 20-m Surface Albedo Retrievals from Sentinel-2A Surface Reflectance and MODIS/VIIRS Surface Anisotropy Measures. *Remote Sens. Environ.* **2018**, *217*, 352–365. [CrossRef]
65. Bauer-Marschallinger, B.; Falkner, K. Wasting Petabytes: A Survey of the Sentinel-2 UTM Tiling Grid and Its Spatial Overhead. *ISPRS J. Photogramm. Remote Sens.* **2023**, *202*, 682–690. [CrossRef]
66. Didan, K.; Munoz, A.B.; Solano, R.; Huete, A. MODIS Vegetation Index User 's Guide (Collection 6). *Univ. Ariz.* **2015**, *2015*, 31.

67. Ulsig, L.; Nichol, C.J.; Huemmrich, K.F.; Landis, D.R.; Middleton, E.M.; Lyapustin, A.I.; Mammarella, I.; Levula, J.; Porcar-Castell, A. Detecting Inter-Annual Variations in the Phenology of Evergreen Conifers Using Long-Term MODIS Vegetation Index Time Series. *Remote Sens.* **2017**, *9*, 49. [CrossRef]
68. Meyer, L.H.; Heurich, M.; Beudert, B.; Premier, J.; Pflugmacher, D. Comparison of Landsat-8 and Sentinel-2 Data for Estimation of Leaf Area Index in Temperate Forests. *Remote Sens.* **2019**, *11*, 1160. [CrossRef]
69. Weiss, M.; Baret, F. *S2ToolBox Level 2 Products: LAI, FAPAR, FCOVER—Version 2.0*; European Space Agency: Paris, France, 2020; pp. 60p. Available online: https://step.esa.int/docs/extra/ATBD_S2ToolBox_V2.0.pdf (accessed on 8 January 2024).
70. Jiang, Z.; Huete, A.R.; Didan, K.; Miura, T. Development of a Two-Band Enhanced Vegetation Index without a Blue Band. *Remote Sens. Environ.* **2008**, *112*, 3833–3845. [CrossRef]
71. Lykhovyd, P.; Averchev, O.; Fedorchuk, M.; Fedorchuk, V. The Relationship between Spatial Vegetation Indices: A Case Study for the South of Ukraine. *Environ. Ecol. Res.* **2023**, *11*, 740–746. [CrossRef]
72. Wickham, J.; Stehman, S.V.; Sorenson, D.G.; Gass, L.; Dewitz, J.A. Thematic Accuracy Assessment of the NLCD 2016 Land Cover for the Conterminous United States. *Remote Sens. Environ.* **2021**, *257*, 112357. [CrossRef]
73. Jin, S.; Homer, C.; Yang, L.; Danielson, P.; Dewitz, J.; Li, C.; Zhu, Z.; Xian, G.; Howard, D. Overall Methodology Design for the United States National Land Cover Database 2016 Products. *Remote Sens.* **2019**, *11*, 2971. [CrossRef]
74. Wickham, J.; Stehman, S.V.; Sorenson, D.G.; Gass, L.; Dewitz, J.A. Thematic Accuracy Assessment of the NLCD 2019 Land Cover for the Conterminous United States. *GIsci Remote Sens* **2023**, *60*. [CrossRef]
75. Yan, L.; Roy, D.P.; Li, Z.; Zhang, H.K.; Huang, H. Sentinel-2A Multi-Temporal Misregistration Characterization and an Orbit-Based Sub-Pixel Registration Methodology. *Remote Sens. Environ.* **2018**, *215*, 495–506. [CrossRef]
76. Lin, G.; Wolfe, R.E.; Zhang, P.; Tilton, J.C.; Dellomo, J.J.; Tan, B. Thirty-Six Combined Years of MODIS Geolocation Trending. In Proceedings of the SPIE 11127, Earth Observing Systems XXIV, San Diego, CA, USA, 9 September 2019; Volume 1112715, pp. 219–230. [CrossRef]
77. Lin, G.; Wolfe, R.E.; Zhang, P.; Dellomo, J.J.; Tan, B. Ten Years of VIIRS On-Orbit Geolocation Calibration and Performance. *Remote Sens.* **2022**, *14*, 4212. [CrossRef]
78. Kern, A.; Marjanović, H.; Barcza, Z. Spring Vegetation Green-up Dynamics in Central Europe Based on 20-Year Long MODIS NDVI Data. *Agric. For. Meteorol.* **2020**, *287*, 107969. [CrossRef]
79. Hassan, Q.K.; Rahman, K.M. Applicability of Remote Sensing-Based Surface Temperature Regimes in Determining Deciduous Phenology over Boreal Forest. *J. Plant Ecol.* **2013**, *6*, 84–91. [CrossRef]
80. Buras, A.; Rammig, A.; Zang, C.S. The European Forest Condition Monitor: Using Remotely Sensed Forest Greenness to Identify Hot Spots of Forest Decline. *Front. Plant Sci.* **2021**, *12*, 689220. [CrossRef]
81. Van Wagtendonk, J.W.; Root, R.R. The Use of Multi-Temporal Landsat Normalized Difference Vegetation Index (NDVI) Data for Mapping Fuel Models in Yosemite National Park, USA. *Int. J. Remote Sens.* **2003**, *24*, 1639–1651. [CrossRef]
82. Furniss, T.J.; Larson, A.J.; Lutz, J.A. Reconciling Niches and Neutrality in a Subalpine Temperate Forest. *Ecosphere* **2017**, *8*, e01847. [CrossRef]
83. Harniss, R.O.; Nelson, D.L. *A Severe Epidemic of Marssonina Leaf Blight on Quaking Aspen in Northern Utah*; USDA Forest Service: Ogden, UT, USA, 1984; pp. 8p.